CJC Chinese Journal of Chemistry 中国化学 - An International Journal

For submission: https://mc.manuscriptcentral.com/cjoc
For published articles: https://onlinelibrary.wiley.com/journal/16147065

Comprehensive Report

Cite this paper: *Chin. J. Chem.* **2023**, *41*, 431—442. **DOI: 10.1002/cjoc.202200542**

A Triethyleneglycol C_{60} Mono-adduct Derivative for Efficient Electron Transport in Inverted Perovskite Solar Cells†

Azhar Fakharuddin,*[‡,a] Konstantina-Kalliopi Armadorou,[‡,b,c] Leandros P. Zorba,[‡,c] Marinos Tountas,[‡,d] Tobias Seewald,[‡,a] Anastasia Soultati,[b] Polychronis Tsipas,[b] Emilia R. Schütz,[a] Nikolaos Tzoganakis,[d] Stylianos Panagiotakis,[b] Konstantina Yannakopoulou,[b] Athanasios Dimoulas,[b] Vassilis Psycharis,[b] Emmanuel Kymakis,[d] Abd Rashid bin Mohd Yusoff,[e] Konstantinos Aidinis,[f,g] Lukas Schmidt-Mende,[a] Georgios C. Vougioukalakis,*[,c] Mohammad Khaja Nazeeruddin,*[,h] and Maria Vasilopoulou*[,b]

[a] *Department of Physics, University of Konstanz, 78457 Konstanz, Germany*
[b] *Institute of Nanoscience and Nanotechnology, National Center for Scientific Research Demokritos, Agia Paraskevi, 15341 Athens, Greece*
[c] *Department of Chemistry, National and Kapodistrian University of Athens, 15771, Athens, Greece*
[d] *Department of Electrical & Computer Engineering, Hellenic Mediterranean University, Estavromenos, Heraklion, GR-71410, Crete, Greece*
[e] *Department of Chemical Engineering, Pohang University of Science and Technology (POSTECH), Pohang, Gyeongbuk 37673, Republic of Korea*
[f] *Department of Electrical and Computer Engineering, Ajman University, P.O. Box 346, Ajman, United Arab Emirates*
[g] *Center of Medical and Bio-allied Health Sciences Research, Ajman, United Arab Emirates*
[h] *Institute of Chemical Sciences and Engineering, École Polytechnique Fédérale de Lausanne (EPFL), Rue de l'Industrie 17, CH-1951 Sion, Switzerland*

Keywords

Electron transport layer | Defect passivation | Biexponential trap filling | Charge transfer | Fullerenes

Comprehensive Summary

Inverted perovskite solar cells (PSCs) have attracted increasing attention in recent years owing to their low-temperature fabrication proces s. However, they suffer from a limited number of electron transport materials available with [6,6]-phenyl C_{61} butyric acid methyl ester (PCBM) to be the most widely studied based on its appropriate energy levels and high electron mobility. The low relative permittivity and aggregation tendency upon illumination of PCBM, however, compromises the solar cell efficiency whereas its modest hydrophobicity negatively impacts on the device stability. Alternative electron transport materials with desired properties and appropriate degree of hydrophobicity are thus desirable for further developments in inverted PSCs. Herein, we synthesize a triethyleneglycol C_{60} mono-adduct derivative (termed as EPF03) and test it as a novel electron transport material to replace PCBM in inverted PSCs based on a quadruple cation (RbCsMAFA) perovskite. We also compare this derivative with two novel fullerenes decorated with two (EPF01) or one dodecyl (EPF02) long side chains. The latter two fail to perform efficiently in inverted PSCs whereas the former enabled a power conversion efficiency of 18.43%, which represents a 9% improvement compared to the reference device using PCBM (17.21%). The enhanced performance mainly stems from improved electron extraction and reduced recombination enabled by the insertion of the large relative permittivity amongst other properties of EPF03. Furthermore, our results indicate that triethylene glycol side chains can also passivate perovskite trap states, suppress ion migration and enhance photostability and long-term stability of EPF03 based perovskite solar cells.

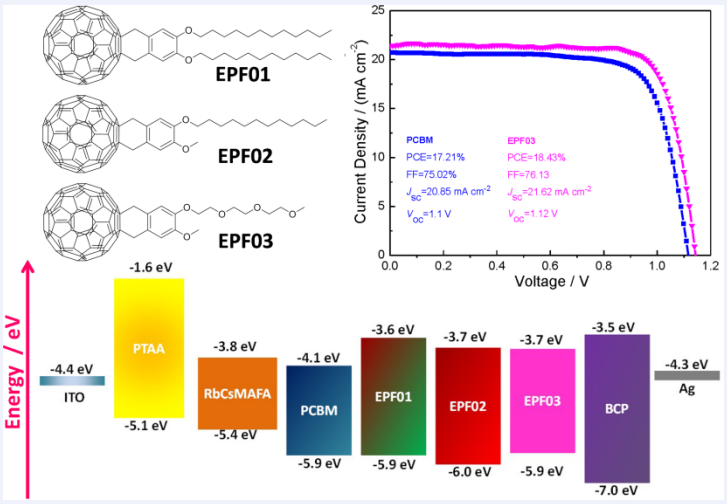

*E-mail: azhar-fakhar.uddin@uni-konstanz.de, vougiouk@chem.uoa.gr, mdkhaja.nazeeruddin@epfl.ch, m.vasilopoulou@inn.demokritos.gr

‡These authors contributed equally to this work.

†Dedicated to the Special Issue of Emerging Investigators in 2022.

Background and Originality Content

In the last decade, hybrid organic-inorganic lead halide perovskites have been attracting considerable attention concerning their application in optoelectronic devices such as solar cells and light emitting diodes. The progress stems mainly from their unique properties including tunable band gap, high absorption coefficient, balanced charge carrier transport, long carrier lifetime, long charge carrier diffusion lengths, high carrier mobilities and small exciton binding energy.[1-9] Accordingly, perovskite solar cells (PSCs) have shown an increase in power conversion efficiency (PCE) from 3.8% to 25.7% in the span of around ten years since their first reports around 2009—2010,[10-11] making them a promising alternative to commercially available crystalline-silicon and inorganic semiconductor thin film solar cells.[12]

A key factor for the high efficiency of PSCs is the suitability of charge transport layers, namely the electron transport layer (ETL) and the hole transport layer (HTL), employed to extract and conduct charge carriers (electrons and holes, respectively) from the perovskite layer to their respective electrodes. 2,2′,7,7′-Tetrakis(*N*,*N*-di-*p*-methoxyphenyl-amine)9,9′-spirobifluorene (Spiro-OMeTAD) is the most common material that acts as HTL in conventional/n-i-p PSCs,[13] owing to its ease of processing in solution, its suitable highest occupied molecular orbital (HOMO) level with respect to the perovskite valence band edge and its high hole mobility. However, its doping requirements,[14] hygroscopic properties, vulnerability to thermal stress, significant voltage losses,[15] and poor adhesion on the perovskite surface[16] are issues that need to be addressed.

In order to overcome the above challenges, inverted PSCs architecture (p-i-n) has been widely adopted.[17-20] The most popular materials used as ETL in inverted PSCs are fullerene-based small molecules, mainly [6,6]-phenyl-C_{61}-butyric acid methyl ester (PCBM).[21-27] Despite its popularity, PCBM still exhibits some disadvantages,[28-30] such as modest hydrophobicity,[31-34] and aggregation issues due to the non-oriented fullerene cage backbone.[35] In addition, its low relative permittivity results in the formation of a large electron capture region, which leads to severe recombination at the interface.[31] Therefore, replacing PCBM with properly functionalized fullerene-based PCBM-like materials is highly desired. These new molecules should be molecularly designed to facilitate electron extraction, have proper energy alignment with the perovskite band edges, and form a smooth homogeneous pinhole-free thin film. These new molecules should also be sufficiently hydrophobic to protect perovskite against moisture ingression, and passivate efficiently the underneath perovskite layer and should offer power conversion efficiency in devices comparable to or higher than the PCBM-based devices.

Towards this direction, fullerene functionalization with appropriate side chain groups has been proposed. Side chains have been found to play a crucial role in the final film structure and transport properties in both fullerenes and conducting polymers.[36-38] The high crystallinity of the resulting films is due to the self-assembling properties and orientation of the side chains of fullerene-based molecules.[39] Amongst the most successful side chains are those including polar groups such as carboxyl, hydroxyl, amine, heterocyclic, and oligoether groups,[40-45] which induce significant increase in the relative permittivity. However, this consideration was neglected during the molecular design in most of the cases,[31] with a notable exception being a C_{60} adduct derivative bearing a triethylene glycol side chain.[44]

In this work, we also demonstrate the successful application of a fullerene derivative bearing a triethyleneglycol side chain (termed as EPF03) as ETL in inverted perovskite structures. The polar character of the glycol group induces a significant increase in the relative permittivity of the EPF03 film compared to that of PCBM, leading to smaller electron capture region, which reduces the nonradiative recombination at the interface between ETL and perovskite. We selected triethyleneglycol instead of ethylene glycol or diethyleneglycol side chains in order to induce a modest degree of hydrophilicity in our fullerene derivative as smaller glycol groups have been found relatively more hydrophilic compared to triethyleneglycol.[46]

To demonstrate the crucial role of the modest hydrophilicity induced by triethyleneglycol group, we also synthesized two other fullerenes bearing one or two long alkyl chains (termed as EPF01-02), which are more hydrophobic. Despite the fact that these derivatives exhibit appropriate energetics and induce surface passivation on the perovskite absorber, they lead to decreased power conversion efficiency (PCE). This mainly stems from a charge accumulation at the perovskite/fullerene interface arising from the large electron capture radius and from their large hydrophobicity, which make them incompatible with the hydrophilic perovskite surface. On the contrary, the less hydrophobic triethyleneglycol fullerene derivative induces improved device performance and stability compared not only to the long alkyl chain fullerenes but also to the commonly used PCBM. This indicates that oligoethyleneglycol side chains with an enhanced flexibility are probably more suitable than alkyl side chains for the design and synthesis of novel fullerene electron transport materials for PSCs.

Results and Discussion

Fullerene derivatives utilized herein were synthesized according to our previously reported synthetic approach, with very minor modifications of the experimental procedures.[24] In brief, the synthesis of intermediates **6**, **7**, and **8** was achieved via Williamson etherification reactions of **3** or **4** with 1-bromododecane (**5**) or γ-bromotriethyleneglycol (**2**), using potassium carbonate and 18-crown-6 in acetone, in very good to excellent yields (Scheme 1). Compounds **9**, **10**, and **11** were received from **6**, **7** or **8**, respectively, with paraformaldehyde and hydrogen bromide dissolved in acetic acid and chloroform, in good to very good yields. Finally, fullerene adducts EPF01, EPF02, and EPF03 were synthesized by reacting intermediates **9**, **10**, or **11**, respectively, with tetrabutylammonium iodide in dry toluene under reflux. These conditions lead to the *in-situ* formation of the corresponding *ortho*-quinodimethanes, which then react with fullerene C_{60}, furnishing the fullerene adducts in moderate yields (Scheme 1).

We further characterized the structural integrity and electronic properties of the synthesized fullerene derivatives and compared them with PCBM by using X-ray photoelectron (XPS) and ultra-violet photoelectron spectroscopy (UPS).[44] Figures S1—S4 (Electronic Supporting Information, ESI) depict the C1s, O1s core level peaks of the different fullerenes used in this study. For the PCBM, the XPS peak fitting reveals a major contribution from C_{60} for the C1s peak, whereas the O1s peak can be deconvoluted in two peaks attributed to methoxy and carbonyl groups. On the contrary, the O1s core level peaks of the EPF01-03 derivatives can be fitted using a single asymmetric peak in accordance to their molecular structure.

From the UPS spectra shown in Figures 1a—d, a slight decrease in the work function (W_F) and small increase in the highest occupied molecular orbital (HOMO) energy of the novel fullerenes compared to PCBM is evident. Similar results are obtained by ambient pressure photoemission (APS) and surface photovoltage (SPV) experiments shown in Figures 2a—e and f, respectively. These measurements were taken in a pristine quadruple cation (RbCsMAFA) perovskite (termed hereafter as PVSK) and PVSK/fullerene films coated on glass and show a significant reduction in the surface W_F of perovskites coated with the novel fullerenes (especially with EPF03). Both, the decreased W_F and higher HOMO energy, can be beneficial for their function as ETLs as they may indicate increased electron extraction and hole blocking properties of these fullerenes compared to the commonly used PCBM.[46-47]

Scheme 1 Synthesis of fullerene adducts EPF01-03.

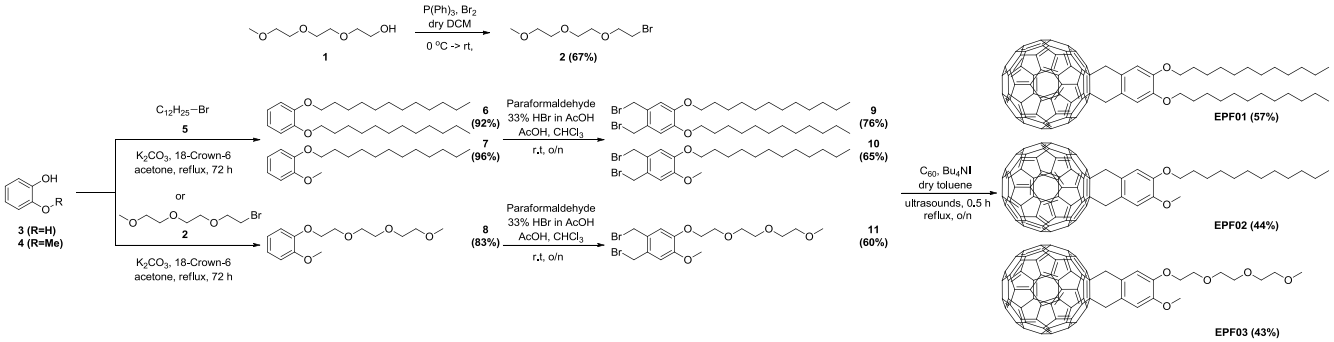

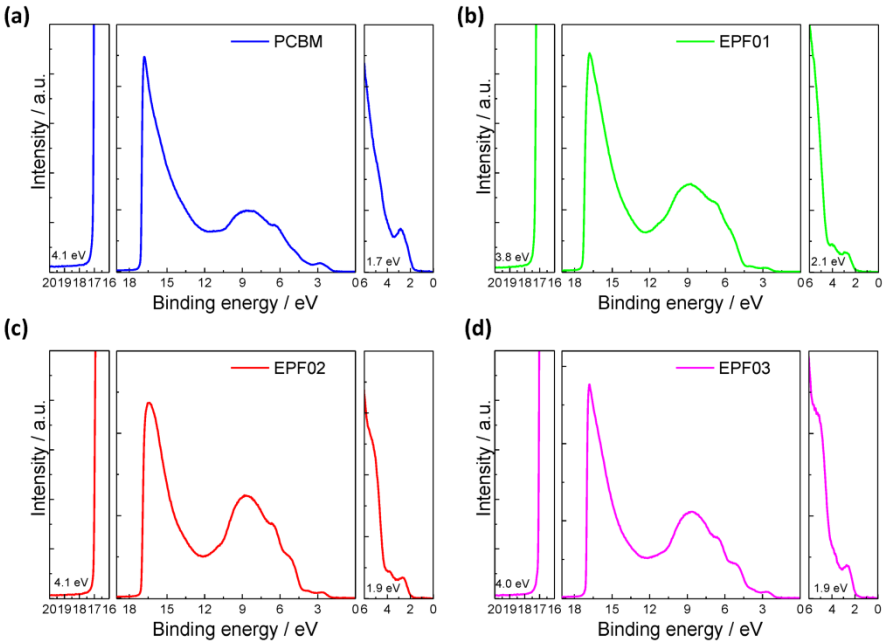

Figure 1 (a—d) The high binding energy electron cut-off region (left), full spectrum (middle) and near Fermi level region (right) of the UPS spectra of the new fullerene derivatives and of the PCBM (for comparison).

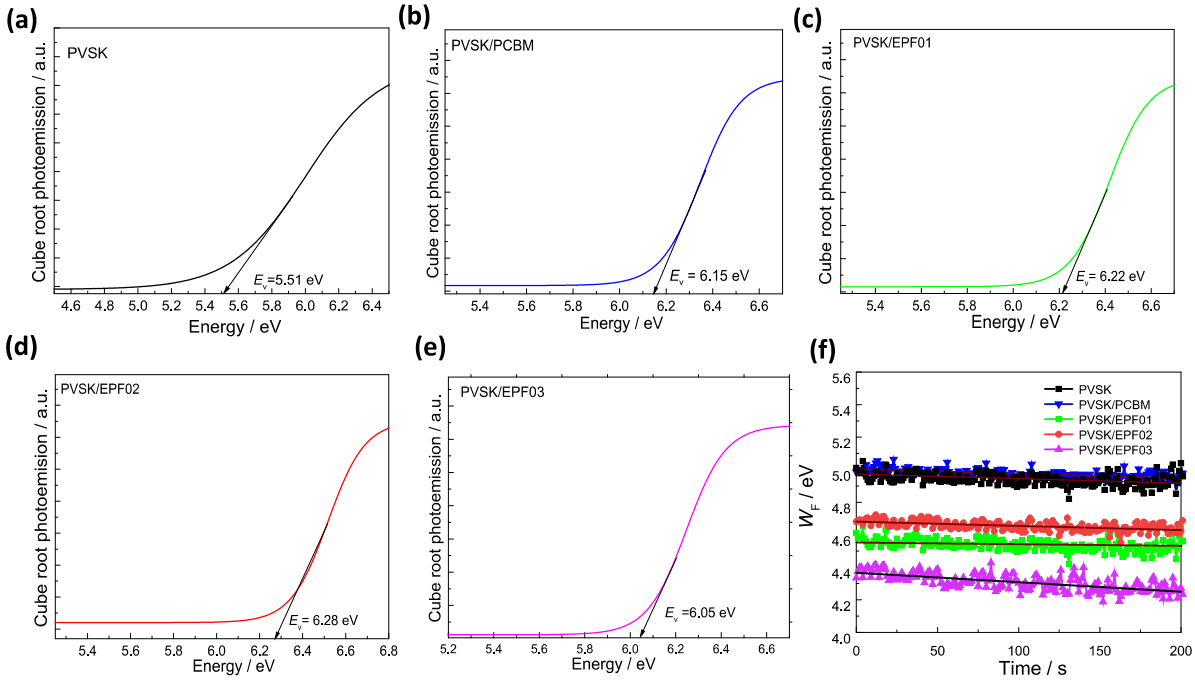

Figure 2 (a—e) Estimation of the valence band maximum of the perovskite without and with PCBM and EPF01-03 atop. (f) Surface W_F of the pristine PVSK and novel EPF01-03 derivatives.

The surface coverage of perovskite by the ETL is a crucial factor in achieving high performance in inverted PSCs. PCBM often displays inhomogeneous film formation, leading to insufficient coverage of the perovskite underlayer. Figures 3a—e show the atomic force microscopy (AFM) images of the above samples measured in air on a scan area of 5 × 5 μm^2. These images reveal the grain formation in the perovskite layer but also the poor coverage by the PCBM film since some of the grains are still distinct. This is not the case for the EPF films, especially for the EPF03 one, where full perovskite coverage is evident. Moreover, PCBM coating, even deposited from a filtered solution (filtered using a PTFE filter with pore size of 0.45 μm) show clustering of particles and non-uniform coverage spots in the film. The EPF01-03 molecules do not show any signs of clustering. Analysis of AFM data shows a root mean square (rms) roughness of 18.4, 13.0, 11.4, 9.9 and 11.2 nm for pristine, PCBM, EPF01, EPF02, and EPF03 samples, respectively. The superior coverage of the perovskite surface with EPF03 is also evident by scanning electron microscopy (SEM) measurements shown in Figure S5. From the X-ray diffraction (XRD) patterns and Fourier transform infrared (FTIR) measurements taken on pristine PVSK and PVSK coated with fullerene films, however, we conclude that these fullerenes have a small impact on the crystallization, whereas they do not affect the composition of the perovskite underlayer (Figure S6).[48-49] Notably, the novel fullerene molecules increase the hydrophobicity of the PVSK surface upon coating as indicated by water static contact angle measurements shown in Figure 3f. This can increase the resistance of the fabricated PSC to the moisture induced degradation.

The interfacial interaction and possible coordination of charge transport materials with the PVSK is of paramount importance as it dictates charge transport, ion migration and defect passivation at the interface. Proton nuclear magnetic resonance (^{1}H NMR) titration experiments were performed to unravel potential surface interaction between the PVSK and fullerene derivatives. These experiments were performed in the polar solvent DMSO-d_6 to investigate the impact of excess perovskite (FAI 1M, MABr 0.22 M, PbI_2 1.1M, PbBr 0.2 M and CsI 1.5 M) on the resonance frequencies of the fullerene derivatives in solution. However, only the less hydrophobic EPF03 from the new fullerenes was completely soluble and amenable to titration (Figures S7, S8), in contrast to the derivatives EPF01 and EPF02 because their hydrophobic alkyl side-chains were insoluble in DMSO-d_6. Titration with the perovskite mixture resulted in rather small chemical shift changes of the EPF03 proton signals (structure numbering shown in Figure 4a) that can be classified in two groups (Figure 4b). The least affected protons ($\Delta\delta$ ~8—12 Hz) were the ones attached to the fullerene ball, namely H2a,b, H2'a,b and H1, which showed a linear dependence (Figure 4b) apparently due to non-specific interactions between the components. The most affected proton signals ($\Delta\delta$ ~18 Hz) were H3 (OMe), H10 (OMe), H9, H6. The chemical shift changes of these protons (Figure 4c) follow a curved graph that does not reach a plateau, despite the large excess (~160-fold) of the titrant. These results indicate that EPF03 binds weakly to perovskite components in solution mainly *via* the protons of the alkoxy side chain and the two terminal methoxy groups, therefore it is plausible to assume that such interactions can be firmly established in the solid state. It has to be noted that the fullerene ball is not observed in the ^{1}H NMR spectrum, thus any involvement of this moiety in the interactions cannot be monitored. The flexible chains of the new fullerene derivatives are expected to improve the film morphology in perovskite solar cells, due to their ability to decrease the degree of aggregation.[50] Furthermore, the interactions mainly of the outer protons of the alkoxy chain of EPF03 with the perovskite mixture in solution suggest that a possibly better charge separation and electron transport capability could be achieved at the interface between fullerene and perovskite, in the solid.

To demonstrate the practical utility of these fullerenes as electron transport materials in PSCs, we next fabricated and tested inverted devices with the structure ITO/PTAA/Perovskite/Fullerene/BCP/Ag, using either PCBM or the new fullerene derivatives as ETLs (Figure 5a). The energy level diagram as derived from UPS and absorption measurements (for the estimation of the energy bandgap value of these materials) is shown in Figure 5b. The current density – voltage (*J-V*) characteristic curves of the best performing PSCs with the PCBM and EPF03 ETLs, under simulated

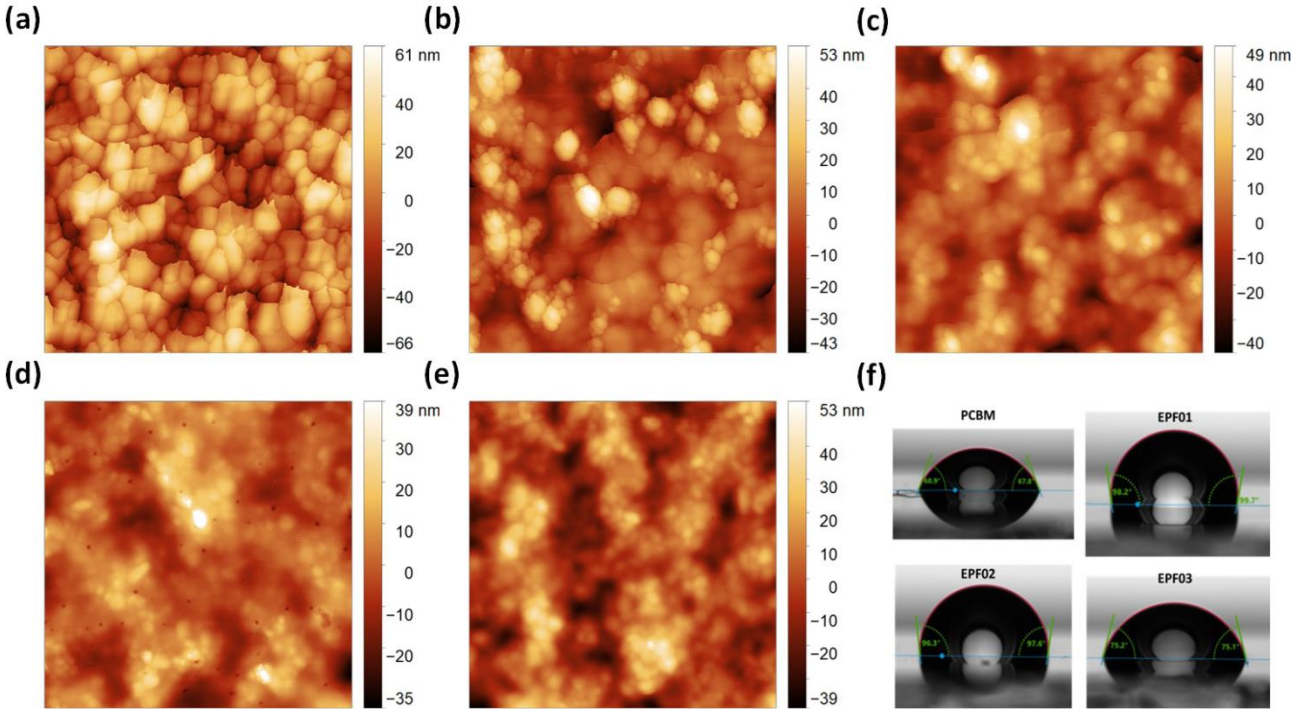

Figure 3 (a—e) 5 x 5 μm^2 2D topographic images of reference perovskite and perovskite coated with PCBM, the new fullerene derivatives (EPF01, EPF02 and EPF03, respectively). (f) Water contact angle measurements taken on PCBM and the new fullerene derivatives.

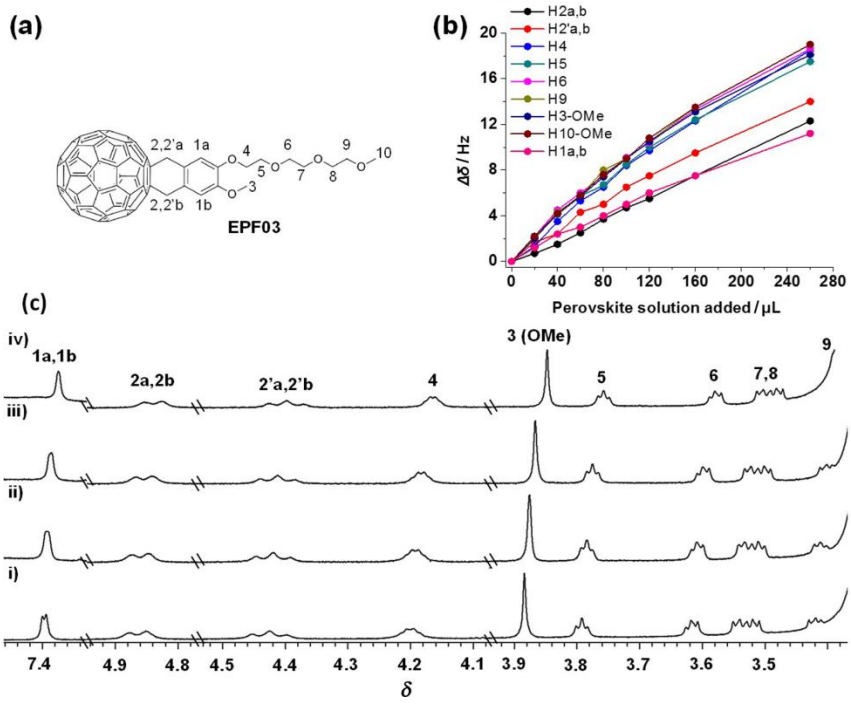

Figure 4 (a) Chemical structure of substituted fullerene derivative EPF03. (b) ^{1}H NMR (500 MHz, 298 K, DMSO-d_6) titration plots and (c) partial stacked spectra of EPF03 (1.3 mg mL^{-1}) after gradual addition (0 to 260 μL) of the perovskite solution (FAI 1 M, MAB 0.22 M, PbI_2 1.1 M, PbBr 0.2 M and CsI 1.5 M). i) + 0 μL, ii) + 40 μL, iii) + 100 μL, iv) + 260 μL.

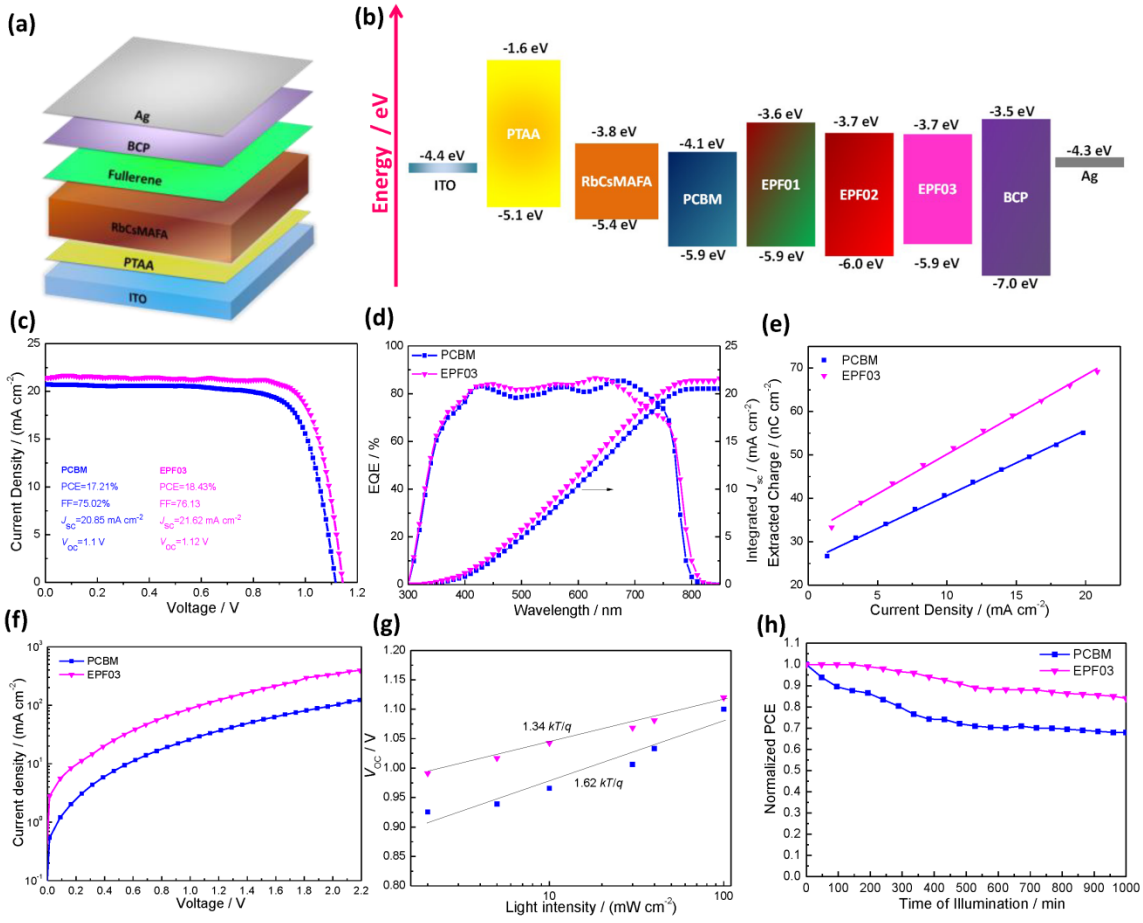

Figure 5 (a) Device structure and (b) energy levels of the different device layers before contact considering vacuum level alignment. (c) Current density-voltage (*J-V*) characteristics of the PSCs using either PCBM or EPF03 as the electron transport material. (d) The EQE measurements along with the integrated photocurrent density and (e) the extracted charge density of the same devices. (f) Current density-voltage characteristics of electron-only devices (ITO/SnO_2/PVSK/PCBM or EPF03/Ag). (g) Variation of V_{OC} versus light intensity and (h) normalized PCE versus time of continuous illumination with 1.5 AM light of unencapsulated PSCs tested in N_2 environment.

AM 1.5G illumination are shown in Figure 5c. The reference device with PCBM as the ETL showed a J_{SC} of 20.85 mA cm^{-2}, a FF of 75.02% and a V_{OC} of 1.1 V, which corresponds to a PCE value of 17.21%. On the other hand, the device with the EPF03 fullerene as the ETL having an optimized concentration of 15 mg mL^{-1} in the precursor solution (Figure S9a which also demonstrates a large process window for EPF03) demonstrated a slightly higher PCE value of 18.43%, caused by a simultaneous enhancement in all three device performance parameters, J_{SC} (21.62 mA cm^{-2}), V_{OC} (1.12 V), and FF (76.13%).

Notably, the performance of the EPF01 and EPF02 using devices was inferior compared to the reference sample (with PCBM) and the EPF03 embedding device (Figure S9b). This result indicates the crucial role of ethyleneglycol side chain in the device performance. The reason behind the inferior device performance using EPF01 and EPF02 could be partly related to high hydrophobicity (higher than that of the commonly used PCBM and EPF03) which implies poor interface quality and poor adhesion with the hydrophilic PVSK. Notably, the EPF03 and PCBM based PSCs were non-hysteretic (Figure S10), very stable when measured at maximum power point (MPP) (Figure S11) and present negligible performance deviation in batches of 16 identical devices of each type (Table S1). The better performance of EPF02 compared to the PCBM embedding device could not mainly stem from difference in the formation of BCP protective underlayer as indicated by the great similarity of AFM topography of BCP on top of the two different fullerene derivatives (Figure S12).

Next, in order to confirm the increase of the J_{SC}, external quantum efficiency (EQE) measurements and the integrated photocurrent densities of the PSCs with PCBM and EPF03 fullerene were measured and are presented in Figure 5d. The change in the EQE graph and the integrated J_{SC} are consistent with the previous values of the calculated J_{SC} from the solar simulator. The enhanced photocurrent obtained in the EPF03 based device was further supported by the increase in extracted charge as a function of current density, taken from transient photocurrent measurements (Figure 5e). The EPF03 fullerene based device, shows a higher extracted charge, *i.e.*, an improved charge collection compared to the reference device with PCBM, which is in agreement with the decreased W_F (implying reduced electron extraction barrier) of this fullerene compared to the other derivatives and PCBM. This might also be related to an enhancement in the electron mobilities/conductivities achieved with the EPF03 compared to PCBM. Figure 5f depicts the current density versus voltage of electron-only devices using either PCBM or EPF03 at the electron extracting contact. The significant enhancement in the electron current in EPF03 devices indicates enhanced electron mobility/conductivity in this case. We argue that the presence of the triethyleneglycol side chain can beneficially affect π-π stacking of the fullerene derivative (as also indicated by the smooth and compact morphology of EPF03 film) thus beneficially altering electron transport towards the selective contact. Better charge transport within the device can also increase the obtained FF, as verified by the PSC measurements.

Besides the improved charge extraction, recombination of the photogenerated carriers is of paramount importance as it dictates energy losses and the achieved performance of the PSC. The carrier recombination in the device was investigated by tracing the change of V_{OC} with the increase of light intensity. Figure 5g shows the plot of V_{OC} versus light intensity. The slope of the device based on pristine PCBM is 1.62 kT/q, which decreases to 1.34 kT/q (where q is the elementary charge, k is the Boltzmann constant, T is the temperature), when using EPF03, implying a significant reduction in trap-assisted recombination,[31] which is important for the optimum device performance. However, not only the achieved efficiency but also the stability of the PSC strongly depends on the recombination losses, as well as, the charge extraction efficiency. As the result of improved electron transport/extraction and reduced recombination, the photostability under continuous 1 sun illumination of the EPF03 based unencapsulated device (tested in N_2 environment) is much improved compared to that with PCBM (Figure 5h). Additionally, due to the higher hydrophobicity of EPF03 compared to that of PCBM, the long-term stability of unencapsulated devices kept in the dark at ambient environment was prolonged (Figure S13).

To further investigate the enhancement in photostability of the EPF03 based PSC, the stability of the PVSK absorber, without and with a fullerene coating, upon exposure to sun light was tested. FTIR spectrum of the pristine perovskite thin film shows a gradual decrease in the intensity of all prominent peaks (Figure S14a). The intensity of the peaks in the 3400—3250 cm^{-1} region (asymmetric and symmetric stretching vibrations of N—H bond in the primary amine unit of methylammonium and formamidinium cations) is decreased constantly throughout the sun exposure process, with the 8 hours' mark being the start of the most obvious change. Similar changes are observed in the peak at 1350 cm^{-1}, corresponding to the bending mode of C—H bond of formamidinium. The intensity of this specific peak is decreased after 8 h of sun exposure, which could be related to the creation of degradation products. The sharp peak at 1710 cm^{-1} due to stretching mode of the C=N bond of the formamidinium unit seems unchanged in terms of intensity after illumination. Other peaks for the pristine perovskite film are located at 1610 cm^{-1} (NH_3 scissoring), at 1470 cm^{-1} (NH_3^+ bending of methylammonium), at 1050 cm^{-1} (N—H rocking), and at 909 cm^{-1} (CH_3-NH_3^+ rocking of methylammonium), whose intensity decreases gradually with increasing exposure time. After 3 h of exposure, a new peak at 1950 cm^{-1} can be observed. This peak can be attributed to the stretching mode of the N-C-N or C-N-C group with partial double bond character (partial carbodiimide character) of *N*-methylformamidinium (MFA) mainly and *N*,*N*-dimethylformamidinium (DMFA) in smaller quantities, which has been reported to be a condensation product from the reaction of methylammonium and formamidinium after aging.[51-52] Since the intensity of this peak increases as all other peaks decrease, we can stipulate that a gradual reaction between formamidinium and methylamine takes place, slowly consuming the initial perovskite moieties towards the formation of the aforementioned decomposition products.

With the deposition of either PCBM or EPF01-03 (Figures S14b—e) on top of the perovskite thin film, similar peaks to the pristine active layer are observed, with a new peak located at 1430 cm^{-1}, attributed to the N—H bending mode of methylammonium. Compared to the reference thin film, this peak has been shifted from 1470 cm^{-1} to 1430 cm^{-1} and has increased in intensity. Indeed, the addition of PCBM or EPF01-03 on top of the perovskite film could be strengthening the N—H bond of methylammonium. Even after illumination, the intensity of this peak remains constant, in contrast to the reference spectrum. This is a sign that incorporating one of those fullerene derivatives in the structure prevents N—H bond cleavage and thus the creation of methylamine and subsequent condensation by-products. Moreover, the spectra of the PVSK/EPF03 film exhibit no changes in terms of intensity or position of peaks even after 10 h of continuous illumination, thus making them comparable to PCBM in terms of its effect on the enhanced photostability of the final thin film. The photostability of perovskite thin films can be further verified through XRD diffraction, where the crystallization of thin films can be observed (Figure S14f). Note that the decreased intensity of the low-angle quadruple perovskite peak at 14.2° in the pristine perovskite compared to the thin films with fullerene derivatives shows the decomposition after exposure.[53-54] Indeed, the degradation can be seen by inactive δ phase peak of the perovskite at 11.7°, which is apparent in the thin films with PCBM and EPF03 but cannot be discerned in the pristine perovskite diffraction pattern. This trend can be seen for all major peaks, located at 20.0°, 28.4°, 30.7° and 39.5°, that are close to the background noise in

the case of pristine perovskite thin film, but are easily observable once fullerene ETLs are deposited, thus confirming their positive effect on the crystallinity of the perovskite layer, as far as their stability under ambient sun exposure is concerned. Notably, the UV-Vis absorption spectra of all fullerene thin films exhibit no changes in terms of intensity or peak position after continuous illumination (Figure S15), which is in agreement with their protecting role to light exposure discussed above.[47,55-61]

In order to gain more insight regarding the charge transport/extraction and recombination using the different fullerenes, we compared the photoluminescence (PL) spectra of the perovskite film on glass coated with the four ETLs (PCBM, EPF01-03) with that of a reference perovskite film (without any ETL on top). The steady state PL spectra (Figure 6a) show a reduction in PL intensity for perovskite films with a fullerene ETL on top, which is attributed to quenching of charge carriers from the perovskite film and facile electron transfer and extraction through the fullerene ETLs. The PCBM, EPF01, EPF02, and EPF03 deposited films lead to 41%, 88%, 92%, and 95% drop in the PL intensity, which suggest that EPF03 is the more efficient ETL to extract electrons from the pristine perovskite film than all other ETLs. Notably, besides the decrease in the PL intensity, a pronounced blue shift in the PL emission peak is observed, when the PVSK layer is coated with the new fullerenes (especially with the EPF03), which is an indication of surface passivation effect of these fullerenes to the perovskite underlayer. The charge extraction kinetics of the fullerene derivatives is further investigated using time-resolved PL (TRPL) measurements of the various ETL/perovskite films (Figure 6b). Fitting TRPL data with a bi-exponential decay to account both for non-radiative recombination caused by defects or surface trap states and the associate charge extraction, as well as, the intrinsic bulk radiative recombination through a shorter and a longer lifetime, respectively, yielded a smaller lifetime for PCBM, EPF01, EPF02, and EPF03 samples than that of the pristine perovskite. In particular, the average lifetime $\langle\tau\rangle$ for reference, PCBM, EPF01, EPF02, and EPF03 samples is 173.5, 31.7, 11.1, 12.99 and 9.1 ns, respectively, indicating a faster electron extraction in the case of EPF03 compared to other fullerenes and, especially, PCBM. This is in agreement with the better device performance by using EPF03.

A key challenge with perovskites is the ion migration and recombination kinetics, which are crucial for the device performance and stability, and can be probed upon continuous illumination of perovskite films. In order to further investigate the photostability of the different ETL coated-perovskite films and to probe slow dynamics due to ion migration and the possible effects the various ETLs might have, we recorded temporal PL of the various perovskite films under continuous exposure to 405 nm pulsed laser (repetition rate 2 MHz, relative humidity of 60%—75%). The evolution of the PL properties, such as change in PL emission intensity, a change in the PL emission peak position and full width at half maxima (FWHM) is shown in Figures 6c—e. The complete dataset for all five samples (reference perovskite without any ETL and perovskite coated with all four ETLs) is shown in Figures S16—S20. One should note that the relative change in the PL intensity for each sample might slightly vary, however, the trend was consistent for different samples measured. From this experiment, a few observations can be drawn. First, the PL intensity rises in a biexponential fashion, where an initial sharp rise followed by a slow increase is evident. This slow rise in the PL intensity has been previously attributed to ion migration.[62-64] Herein, upon exposure to light, ions diffuse away from the region under light illumination. During movement, ions remove and passivate defect sites on their way thus leading to a higher radiative recombination. An important factor is the photoexcited carrier, which has shown to deactivate defect sites more effectively in the presence of oxygen.[65] Another important observation is the drop in the PL intensity, which is due to the degradation of perovskite films in air.[66-67] Figures 6c—e show clearly the competing processes

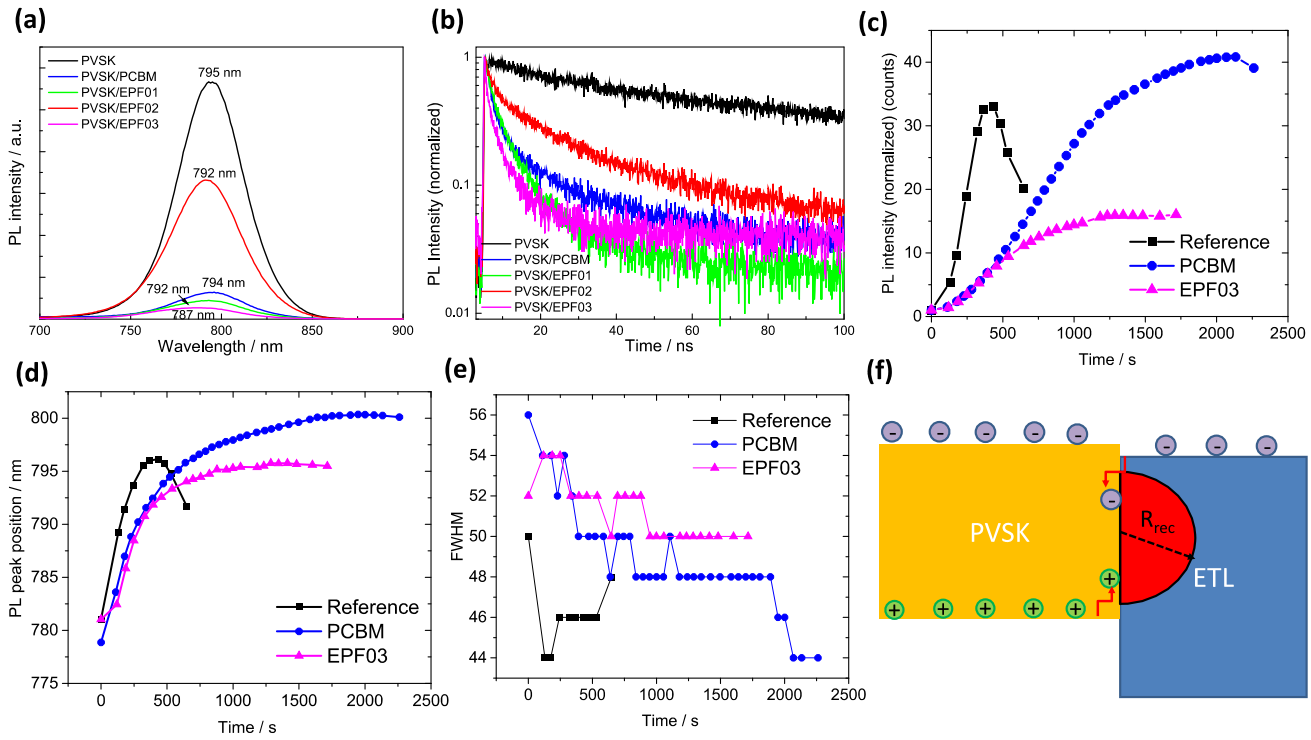

Figure 6 (a) Photoluminescence spectra of perovskite/fullerene derivatives films and (b) time-resolved PL decay transients measured at the peak emission wavelength for the same films after excitation at 405 nm. The films were deposited on glass substrates and the measurements were performed at the air (film) side. Temporal evolution of photoluminescence properties of the various perovskite films. (c) Variation in the PL intensity over time, (d) shift in the PL emission peak position, and (e) change in full width at half maxima (FWHM) of the reference perovskite film (without any ETL on top), perovskite films coated with PCBM and EPF03 ETL on top. The samples are measured under continuous exposure to laser irradiation and multiple PL spectra are recorded to note the emission properties. (f) Diagram for the mechanism of carrier recombination at the interface between perovskite and ETL.

of defect-healing due to ion migration and the degradation, the degree of which varies for the different samples. All the samples show a red shift in the PL intensity (Figure 6d), which suggests a change in the chemical composition (phase segregation in this complex multi-cation perovskite) of the perovskite film upon light soaking. One can note the different degree of changes in the spectral shapes of these perovskite films (Figures S16—20). For reference perovskite, emission from an intermediate band at around 700 nm becomes apparent upon light soaking (visible in log plots of the PL emission). The ETL coated samples do not show emission from any additional band, which indicates negligible or no change in the chemical composition of the perovskite films, an effect which is more pronounced in the EPF01-03 samples. This result is in accordance with the FTIR degradation study shown above.

Since that all these samples have in common the same perovskite material, the rise in the PL intensity is qualitatively correlated to the defect density in the various films.[67] This suggests a higher defect density in the PCBM coated perovskite film than its EPF03-counterpart, where less non-radiative recombination is accounted. Unfortunately, a comparison with reference perovskite film is not possible as degradation takes over with first 300 s (although one can note that the initial rise in the PL intensity was the highest/fastest in the reference perovskite film). Notably, the ETL coated perovskite films show either no signs of degradation or a slight degradation after several minutes, evidencing that the ETL capping layer acts as a barrier to moisture/oxygen thus improving film stability in ambient condition.

To also explain the less non-radiative recombination at perovskite/EPF03 interface, we evaluate the relative permittivity of PCBM and EPF03 by capacitance versus frequency measurements in parallel plate capacitors with PCBM or EPF03 films between the two plates (Figure S21). A relative permittivity of 3.8 for PCBM and of 4.5 for EPF03 was estimated. The large enhancement in relative permittivity (ε_r) for EPF03 is important as it defines a smaller electron capture region, which is the region where photogenerated electrons and holes interact with electrostatic forces.[31,44] This region is assumed to be a function of critical radius (R_c) calculated by the equation: $R_c = q^2/4\pi kT\varepsilon_0\varepsilon_r$, where ε_0 and ε_r are the vacuum permittivity and relative permittivity of the ETL, respectively. Increasing ε_r can reduce the R_c, resulting in smaller electron capture region and reduced recombination as illustrated in Figure 6f. This also indicates that the photogenerated carriers can more easily escape from the large part of the photoabsorber layer as they do not interact electrostatically with each other. As a result, the charge extraction can be potentially enhanced.

Finally, in order to further understand charge kinetics of the various perovskite films with ETL on top, we carried out transient absorption (TA) spectroscopy in air (Figure 7). We note a reduction in initial signal amplitude from the bandgap bleach of the perovskite (Figure S22), when ETLs are deposited on top. We attribute this to a lower excitation density due to parasitic absorption in the fullerenes and possibly some contribution from Fresnel reflection from the additional optical interface, as the films are excited from the top side (with excited light reaching fullerene first). During excitation, the charges created in the fullerene can be transferred into the perovskite, leading to a rise in the TA signal from the perovskite. This effect is most pronounced for the EPF01/perovskite film, which has the highest LUMO offset to the PVSK conduction band minimum, therefore electron transfer is energetically most favorable. The relative magnitude of the effect, however, inversely correlates to the device performance parameters since electron transfer in this direction is undesirable for solar cell operation.

3. Conclusions

In conclusion, a novel C_{60} fullerene derivative bearing a triethyleneglycol side chain outperforms as an electron transport material the commonly used PCBM and two C_{60} compounds with one or two long alkyl side chains. It is used to replace PCBM in inverted (p-i-n) PSCs based on a quadruple cation perovskite (RbCsMAFA) enabling a PCE of 18.43%, which is better than that of the reference device using PCBM (17.21%). This is mainly attributed to the enhanced electron extraction enabled by the insertion of a thin EPF03 layer atop the perovskite absorber along with a passivation effect on the perovskite surface trap states. Moreover, reduced recombination is concluded from a decrease in the electron caption region as derived from an increase in relative permittivity of EPF03 compared to PCBM. The device photostability is also enhanced due to the excellent light protecting properties of this fullerene. This work aims to provide design rules for the synthesis of functionalized fullerenes with advanced electron extraction and transport properties in perovskite solar cells and related optoelectronics.

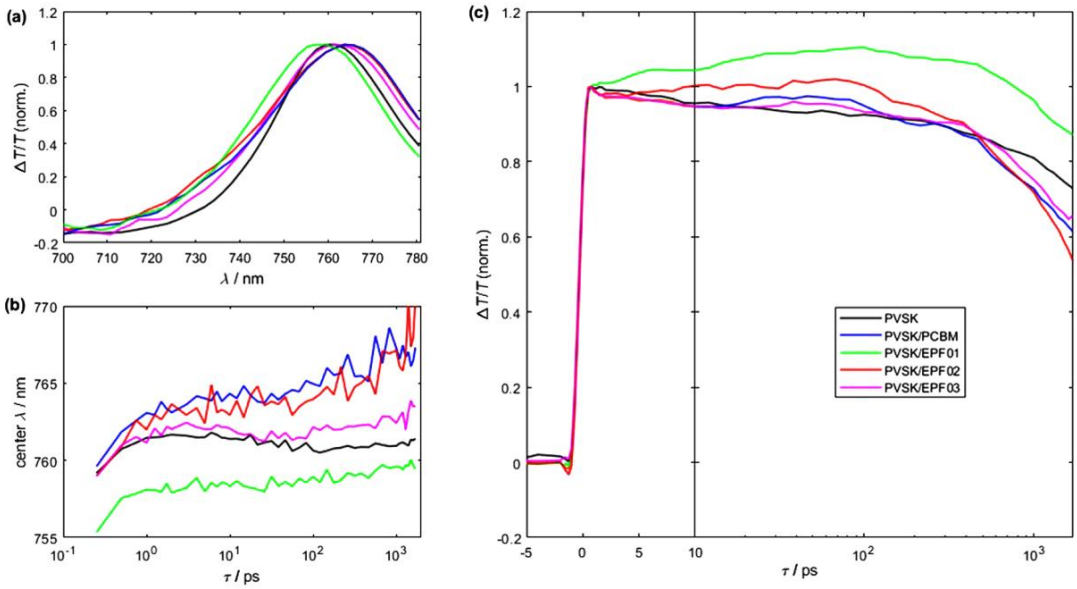

Figure 7 (a) Transient absorption spectra at 5 ps pump-probe delay, (b) evolution of the peak wavelength, and (c) the amplitude at the peak wavelength with pump-probe delay (normalized to initial peak at 0.75 ps).

Experimental

Materials and solvents

Poly[bis(4-phenyl)(2,4,6-trimethylphenyl)amine] (PTAA) was purchased from Solaris (M_w = 20—70 kDa). [6,6]-phenyl C_{61} butyric acid methyl ester (PCBM) was purchased from Solenne BV and bathocuproine (BCP) from Sigma-Aldrich. The materials for the perovskite layer formation, *e.g.*, PbI_2 and $PbBr_2$ (99.99% purity) were obtained from TCI, FAI and MABr were purchased from GreatCell Solar. CsI (99.999%) was bought from Alfa Aesar and RbI (99.8%) was obtained from Sigma-Aldrich. Dimethyl sulfoxide (DMSO, anhydrous ≥ 99.9%), dimethylformamide (DMF, anhydrous 99.8%), and chlorobenzene (CB, anhydrous 99.8%) were purchased from Sigma-Aldrich. Toluene 99.7% and isopropanol (IPA) > 99.8% were obtained from Honeywell Research Chemicals.

Fabrication of inverted PSCs

Indium tin oxide (ITO)/glass patterned substrates (ITO thickness of 100 nm and a sheet resistance of 20 Ω/sq purchased from Ossila) were sequentially cleaned with soap water, deionized water, acetone, and isopropanol with ultrasonication for 10 min each. Afterwards, the substrates were transferred in a N_2 filled glovebox and underwent a UV-ozone treatment for 15 min. The hole transport layer was developed by a PTAA solution (2mg mL^{-1} in toluene), which was spin-coated on ITO substrates at 6000 r/min for 30 s and then annealed at 110 °C for 10 min. For the perovskite precursor solution, 1.24 M PbI_2 (9% excess), 1.14 M FAI, 0.2 M $PbBr_2$ and 0.2 M MABr were dissolved in DMF : DMSO 4 : 1 and then 5 vol% CsI and 4 vol% RbI from 1.5 M stock solutions dissolved in DMF and DMF : DMSO 4 : 1, respectively were added, in order to obtain the 4-cation perovskite composition $Rb_{0.04}Cs_{0.05}(FA_{0.85}MA_{0.15})_{0.91}Pb(I_{0.85}Br_{0.15})_3$. The perovskite layer was deposited by dynamically spinning the solution on the PTAA film at 6000 r/min for 45 s. After 25 s of the start of spin-coating process antisolvent treatment was applied dropping 200 μL of antisolvent (anhydrous CB) on the samples. Then, the as-prepared perovskite film was immediately placed on a hot-plate and annealed at 100 °C for 45 min. The PCBM and/or fullerene derivatives (EPF01, EPF02, and EPF03) serving as the electron transport layer (ETL) were formed by spinning a PCBM solution in anhydrous CB with concentration of 20 mg mL^{-1}, and/or EPF solution (various concentrations in anhydrous CB) at 2000 r/min for 60 s and left to dry in the N_2 filled glovebox at room temperature for 30 min. On top of the ETL, a thin buffer layer of bathocuproine (BCP, 0.5 mg mL^{-1}) in IPA was dynamically spin-coated at 4000 r/min for 45 s. Finally, a 100 nm-thick Ag top electrode was deposited by thermal evaporation under a high vacuum (4×10^{-6} mbar).

Thin film and device characterization

Ultra-violet photoemission spectroscopic (UPS) measurements were performed using the He I excitation line (21.2 eV) with a negative bias of 12.22 V applied to the specimen in order to separate the high binding energy cut-off from the analyzer. A Bruker Tensor 27 FT-IR spectrometer equipped with a DTGS detector was used to take Fourier-transform infrared (FT-IR) transmittance spectra of the different fullerene electron transport materials deposited on the perovskite layer. UV-Vis absorption measurements of the different ETLs, as well as, of the perovskite layer with different ETLs coatings were obtained using a Perkin Elmer Lambda 40 spectrometer. Scanning electron microscopy (SEM) images of the RbCsMAFA films coated with different fullerenes were recorded with a JSM-7610F-Schottky Field Emission ultra-high resolution Scanning Electron Microscope (JEOL). Atomic force microscopy (AFM) measurements were performed using an NX 10 AFM (Park Systems) in air in a true non-contact mode. To study the crystallinity of the perovskite films, X-ray diffraction measurements were performed using an X-ray Siemens D-500 606 diffractometer. Photoluminescence (PL) spectra of the perovskite films used in the inverted PSCs were taken using a 450 nm laser diode module and a Si photodiode and analyzed with an Oriel 77200 monochromator. Current density-voltage (*J-V*) characteristics curves of the inverted PSCs were recorded using an Autolab PG-STAT-30 potentiostat (1 sun, 100 mW cm^{-2}) including an AM 1.5G filter. The EQE spectra of the prepared devices were taken using an Autolab PG-STAT-30 measurement system equipped with an Oriel 1/8 monochromator and a 300 W Xe lamp, and the light intensity at each wavelength was calibrated with a standard single-crystal Si photovoltaic cell. The device active area of around 0.04 cm^2 was defined using a black metallic aperture mask. Transient photovoltage and transient photocurrent measurements were performed with a commercial apparatus (Arkeo, Cicci Research s.r.l.) based on a high-speed Waveform Generator that drives a highspeed LED (5000 Kelvin). The device is connected to a trans-impedance amplifier and a differential voltage amplifier to monitor short-circuit current or open-circuit voltage. The light intensity from the pulse is varied between 0.001—2 sun equivalent. For transient photovoltage, the perturbation produced by the LED is less than 10% of the background applied light bias. Transient photocurrent measurements were performed under large perturbations (Duty cycle 0.3) for a time duration of 400 μs. The devices are connected to a 50 Ω and 1 MΩ resistor for TPC and TPV measurements, respectively. Ambient photoemission spectroscopy (APS) was conducted with an APS04 N2-RH system (KP Technology). Contact potential difference (CPD) was measured by the vibrating gold alloy Kelvin probe (2 mm). Absolute W_F of the tip was estimated to be around 4.54—4.6 eV, which was calibrated by measuring a silver reference and calculating its absolute W_F by APS.

Photoluminescence, time-resolved PL and transient absorption measurements

The PL and TRPL measurements were carried out in air at a relative humidity between 60%—75% without any encapsulation of protective layer on the perovskite films. The spectra were recorded using a PicoQuant FluoTime300 fluorescence spectrometer using a 405 nm pulsed excitation laser. The repetition rate was set to 80 MHz for steady state- and 2 MHz for TRPL measurements. A long pass filter (455 nm) was used during the measurements to cut-off incoming (scattered) laser light. The temporal PL was recorded by keeping the sample under continuous exposure to light and multiple spectra were recorded (one spectrum per 1—2 min) until the sample either reaches a steady-state or shows a sign of degradation (a drop in the PL intensity).

Transient absorption spectroscopy was performed on a home-built setup based on a regeneratively amplified titanium:sapphire laser system (Mira 900 & RegA 9000, Coherent) producing 150 fs pulses centered at 800 nm at a repetition rate of 200 kHz. A portion of the beam is focused into a sapphire plate to produce a white light continuum used as the probe, while the pump is frequency-doubled in a BBO crystal and sent over a delay stage. The excitation at 400 nm is attenuated to a fluence of 1.5 μJ/cm², well below the degradation threshold of the perovskite films. The transmitted probe beam is detected with an imaging spectrograph (Kymera 193i & Zyla5.5, Andor), electronically synchronized to a 276 Hz dual-chopping scheme, acquiring 3000 spectra per delay.

Ambient Pressure Photoemission Spectroscopy (APS) and Surface Photovoltage (SPV)

The APS and SPV measurements were performed by an APS04-NH2 system (KP Technology) on samples prepared on cleaned ITO substrates. During the measurements, the ITO substrate was connected to the ground. The valence band edge of the semiconductor layers was determined by scanning the UV light excitation in the range of 4.8—6.2 e V (D2 lamp) and extrapolating the cube root photoemission to zero. Fermi level of the samples was calculated from the contact potential difference measured by

the vibrating top Kelvin probe (2 mm, gold alloy tip) and from the work function of the tip (around 4.5—4.6 eV), which was determined using a silver reference. The samples were kept and prepared in the dark (or minimal light condition) for SPV measurements. Before the measurement was taken, the dark work function was monitored until a stable signal was reached. Then, the sample was illuminated with white light (20 mW cm^{-2}) for 50 s and the SPV decay was recorded for further 50 s.

NMR studies

^{1}H and 2D NMR spectra were recorded on a Bruker Avance 500 MHz spectrometer in DMSO-d_6 or in $CDCl_3$ solutions using the residual solvent signal as the internal standard and were processed with Topspin 4.0.8. The assignment of the resonance signals to the structure of the compounds was performed based on the COSY and HSQC data and on the NMR information in $CDCl_3$ reported previously.[47] A dilute solution of the fullerene derivative EPF03 (1.3 mg mL^{-1}, 4.8 mM) and a concentrated perovskite solution (FAI 1 M, MAB 0.22 M, PbI_2 1.1 M, PbBr 0.2 M and CsI 1.5 M) in DMSO-d_6 were prepared. The EPF03 solution was then titrated with the perovskite solution, added in small aliquots (20 to 260 µL). Each time the ^{1}H NMR spectrum was recorded. The resulting chemical shift changes ($\Delta\delta$) were registered and plotted against the perovskite volume added. The same experiments were attempted with EPF01 and EPF02. However, due to their very low solubility in DMSO-d_6 these compounds did not show satisfactory ^{1}H NMR spectra (not shown) and thus titration experiments were not performed.

Supporting Information

The supporting information for this article is available on the WWW under https://doi.org/10.1002/cjoc.202200542.

Aknowledgements

T.S. and E.R.S acknowledge funding from the DFG in the frame of the SPP2196 (project numbers 424156582 and 423660474). G.C.V. and L.P.Z. acknowledge funding provided by the Special Account for Research Grants of the National and Kapodistrian University of Athens (research projects 14872, 16294, 16598, 17168, and 17784). Dr. Eleftherios K. Pefkianakis and Anastasios Misichronis are acknowledged for some initial contributions in the synthesis of the fullerene derivatives. This work was also supported by the research project “HELIOKERAMOS” - MIS 5066858, funded by the Operational Programme (EPAnEK) "Competitiveness, Entrepreneurship and Innovation" (NSRF 2014-2020), under the special action "Industrial Materials" and co-financed by Greece and the European Union (European Regional Development Fund).

References

[1] Zhao, D.; Chen, C.; Wang, C.; Junda, M. M.; Song, Z.; Grice, C. R.; Yu, Y.; Li, C.; Subedi, B.; Podraza, N. J.; Zhao, X.; Fang, G.; Xiong, R.-G.; Zhu, K.; Yan, Y. Efficient two-terminal all-perovskite tandem solar cells enabled by high-quality low-bandgap absorber layers. *Nat. Energy* **2018**, *3*, 1093–1100.

[2] Wehrenfennig, C.; Eperon, G. E.; Johnston, M. B.; Snaith, H. J.; Herz, L. M. High Charge Carrier Mobilities and Lifetimes in Organolead Trihalide Perovskites. *Adv. Mater.* **2014**, *26*, 1584–1589.

[3] Shi, D.; Adinolfi, V.; Comin, R.; Yuan, M.; Alarousu, E.; Buin, A.; Chen, Y.; Hoogland, S.; Rothenberger, A.; Katsiev, K.; Losovyj, Y.; Zhang, X.; Dowben, P. A.; Mohammed, O. F.; Sargent, E. H.; Bakr, O. M. Low trap-state density and long carrier diffusion in organolead trihalide perovskite single crystals. *Science* **2015**, *347*, 519–522.

[4] Dong, Q.; Fang, Y.; Shao, Y.; Mulligan, P.; Qiu, J.; Cao, L.; Huang, J. Electron-hole diffusion lengths >175 µm in solution-grown $CH_3NH_3PbI_3$ single crystals. *Science* **2015**, *347*, 967–970.

[5] Jesper Jacobsson, T.; Correa-Baena, J.-P.; Pazoki, M.; Saliba, M.; Schenk, K.; Grätzel, M.; Hagfeldt, A. Exploration of the compositional space for mixed lead halogen perovskites for high efficiency solar cells. *Energ. Environ. Sci.* **2016**, *9*, 1706–1724.

[6] Xing, G.; Mathews, N.; Sun, S.; Lim, S. S.; Lam, Y. M.; Graẗzel, M.; Mhaisalkar, S.; Sum, T. C. Long-range balanced electron- and hole-transport lengths in organic-inorganic $CH_3NH_3PbI_3$. *Science* **2013**, *342*, 344–347.

[7] Ponseca, C. S.; Savenije, T. J.; Abdellah, M.; Zheng, K.; Yartsev, A.; Pascher, T.; Harlang, T.; Chabera, P.; Pullerits, T.; Stepanov, A.; Wolf, J.-P.; Sundström, V. Organometal Halide Perovskite Solar Cell Materials Rationalized: Ultrafast Charge Generation, High and Microsecond-Long Balanced Mobilities, and Slow Recombination. *J Am. Chem. Soc.* **2014**, *136*, 5189–5192.

[8] Fakharuddin, A.; Gangishetty, M. K.; Abdi-Jalebi, M.; Chin, S.-H.; bin Mohd Yusoff, A. R.; Congreve, D. N.; Tress, W.; Deschler, F.; Vasilopoulou, M.; Bolink, H. J. Perovskite light-emitting diodes. *Nat. Electron.* **2022**, *5*, 203–216.

[9] Leng, K.; Abdelwahab, I.; Verzhbitskiy, I.; Telychko, M.; Chu, L.; Fu, W.; Chi, X.; Guo, N.; Chen, Z.; Chen, Z.; Zhang, C.; Xu, Q.-H.; Lu, J.; Chhowalla, M.; Eda, G.; Loh, K. P. Molecularly thin two-dimensional hybrid perovskites with tunable optoelectronic properties due to reversible surface relaxation. *Nat. Mater.* **2018**, *17*, 908–914.

[10] Kojima, A.; Teshima, K.; Shirai, Y.; Miyasaka, T. Organometal Halide Perovskites as Visible-Light Sensitizers for Photovoltaic Cells. *J. Am. Chem. Soc.* **2009**, *131*, 6050–6051.

[11] NREL, Best cell efficiency chart. Retrieved on 8.8.2022. **2022**.

[12] Rong, Y.; Hu, Y.; Mei, A.; Tan, H.; Saidaminov, M. I.; Seok, S. I.; McGehee, M. D.; Sargent, E. H.; Han, H. Challenges for commercializing perovskite solar cells. *Science* **2018**, *361*, eaat8235.

[13] Lee, M. M.; Teuscher, J.; Miyasaka, T.; Murakami, T. N.; Snaith, H. J. Efficient Hybrid Solar Cells Based on Meso-superstructured Organometal Halide Perovskites. *Science* **2012**, *338*, 643–647.

[14] Leijtens, T.; Ding, I.-k.; Giovenzana, T.; Bloking, J. T.; McGehee, M. D.; Sellinger, A. Hole transport materials with low glass transition temperatures and high solubility for application in solid-state dye-sensitized solar cells. *ACS Nano* **2012**, *6*, 1455–62.

[15] Schulz, P.; Edri, E.; Kirmayer, S.; Hodes, G.; Cahen, D.; Kahn, A. Interface energetics in organo-metal halide perovskite-based photovoltaic cells. *Energ. Environ. Sci.* **2014**, *7*, 1377–1381.

[16] Yue, Y.; Salim, N.; Wu, Y.; Yang, X.; Islam, A.; Chen, W.; Liu, J.; Bi, E.; Xie, F.; Cai, M.; Han, L. Enhanced Stability of Perovskite Solar Cells through Corrosion-Free Pyridine Derivatives in Hole-Transporting Materials. *Adv. Mater.* **2016**, *28*, 10738–10743.

[17] Rombach, F. M.; Haque, S. A.; Macdonald, T. J. Lessons learned from spiro-OMeTAD and PTAA in perovskite solar cells. *Energ. Environ. Sci.* **2021**, *14*, 5161–5190.

[18] Malinkiewicz, O.; Yella, A.; Lee, Y. H.; Espallargas, G. M.; Graetzel, M.; Nazeeruddin, M. K.; Bolink, H. J. Perovskite solar cells employing organic charge-transport layers. *Nat. Photon.* **2014**, *8*, 128–132.

[19] Guo, F.; Li, N.; Fecher, F. W.; Gasparini, N.; Quiroz, C. O. R.; Bronnbauer, C.; Hou, Y.; Radmilović, V. V.; Radmilović, V. R.; Spiecker, E.; Forberich, K.; Brabec, C. J. A generic concept to overcome bandgap limitations for designing highly efficient multi-junction photovoltaic cells. *Nat. Commun.* **2015**, *6*, 7730.

[20] Schmidt-Mende, L.; Dyakonov, V.; Olthof, S.; Ünlü, F.; Lê, K. M. T.; Mathur, S.; Karabanov, A. D.; Lupascu, D. C.; Herz, L. M.; Hinderhofer, A.; Schreiber, F.; Chernikov, A.; Egger, D. A.; Shargaieva, O.; Cocchi, C.; Unger, E.; Saliba, M.; Byranvand, M. M.; Kroll, M.; Nehm, F.; Leo, K.; Redinger, A.; Höcker, J.; Kirchartz, T.; Warby, J.; Gutierrez-Partida, E.; Neher, D.; Stolterfoht, M.; Würfel, U.; Unmüssig, M.; Herterich, J.; Baretzky, C.; Mohanraj, J.; Thelakkat, M.; Maheu, C.; Jaegermann, W.; Mayer, T.; Rieger, J.; Fauster, T.; Niesner, D.; Yang, F.; Albrecht, S.; Riedl, T.; Fakharuddin, A.; Vasilopoulou, M.; Vaynzof, Y.; Moia, D.; Maier, J.; Franckevičius, M.; Gulbinas, V.; Kerner, R. A.; Zhao, L.; Rand, B. P.; Glück, N.; Bein, T.; Matteocci, F.; Castriotta, L. A.; Carlo, A. D.;

Scheffler, M.; Draxl, C. Roadmap on organic–inorganic hybrid perovskite semiconductors and devices. *APL Mater.* **2021**, *9*, 109202.
[21] Jeng, J. Y.; Chiang, Y. F.; Lee, M. H.; Peng, S. R.; Guo, T. F.; Chen, P.; Wen, T. C. $CH_3NH_3PbI_3$ perovskite/fullerene planar-heterojunction hybrid solar cells. *Adv. Mater.* **2013**, *25*, 3727–3732.
[22] Sun, S.; Salim, T.; Mathews, N.; Duchamp, M.; Boothroyd, C.; Xing, G.; Sum, T. C.; Lam, Y. M. The origin of high efficiency in low-temperature solution-processable bilayer organometal halide hybrid solar cells. *Energ. Environ. Sci.* **2014**, *7*, 399–407.
[23] Docampo, P.; Ball, J. M.; Darwich, M.; Eperon, G. E.; Snaith, H. J. Efficient organometal trihalide perovskite planar-heterojunction solar cells on flexible polymer substrates. *Nat. Commun.* **2013**, *4,* 2761.
[24] Pefkianakis , E. K.; Manthou, V. S.; Paraskevopoulou, P.; Sakellariou, G.; Vougioukalakis, G. C. A New Family of Fullerene Derivatives Bearing Long Alkyl and Triethyleneglycol Moieties. *ChemistrySelect* **2016**, *1*, 1232–1238.
[25] You, J.; Hong, Z.; Yang, Y.; Chen, Q.; Cai, M.; Song, T.-B.; Chen, C.-C.; Lu, S.; Liu, Y.; Zhou, H.; Yang, Y. Low-Temperature Solution-Processed Perovskite Solar Cells with High Efficiency and Flexibility. *ACS Nano* **2014**, *8*, 1674–1680.
[26] Jiang, J.; Wang, J.; Zai, H.; Ni, D.; Wang, J.; Xue, P.; Li, N.; Jia, B.; Lu, H.; Zhang, Y.; Wang, F.; Guo, Z.; Bi, Z.; Xie, H.; Wang, Q.; Ma, W.; Tu, Y.; Zhou, H.; Zhan, X. Reducing Energy Disorder in Perovskite Solar Cells by Chelation. *J. Am. Chem. Soc.* **2020**, *144*, 5400–5410.
[27] Li, X.; Zhang, W.; Guo, X.; Lu, C.; Wei, J.; Fang, J. Construting Heterojunctions by Surface Sulfidation for Efficient Inverted Perovskite Solar Cells. *Science* **2022**, *375*, 434–437.
[28] Xiao, D.; Wang, D.-M.; Li, X.; Li, Q.; Shen, K.; Wang, D.-Z.; Wu, L.-L.; Wang, D.-L. Nickel oxide as back surface field buffer layer in CdTe thin film solar cell. *Acta Phys. Sinica* **2017**, *66*, 117301.
[29] Seo, J.; Park, S.; Chan Kim, Y.; Jeon, N. J.; Noh, J. H.; Yoon, S. C.; Seok, S. I. Benefits of very thin PCBM and LiF layers for solution-processed p-i-n perovskite solar cells. *Energ. Environ. Sci.* **2014**, *7*, 2642–2646.
[30] Bai, Y.; Yu, H.; Zhu, Z.; Jiang, K.; Zhang, T.; Zhao, N.; Yang, S.; Yan, H. High performance inverted structure perovskite solar cells based on a PCBM: polystyrene blend electron transport layer. *J. Mater. Chem. A* **2015**, *3*, 9098–9102.
[31] Yang, D.; Zhang, X.; Wang, K.; Wu, C.; Yang, R.; Hou, Y.; Jiang, Y.; Liu, S.; Priya, S. Stable Efficiency Exceeding 20.6% for Inverted Perovskite Solar Cells through Polymer-Optimized PCBM Electron-Transport Layers. *Nano Lett* **2019**, *19*, 3313–3320.
[32] Xiong, J.; Qi, Y.; Zhang, Q.; Box, D.; Williams, K.; Tatum, J.; Das, P.; Pradhan, N. R.; Dai, Q. Enhanced Moisture and Water Resistance in Inverted Perovskite Solar Cells by Poly(3-hexylthiophene). *ACS Appl. Energy Mater.* **2021**, *4*, 1815–1823.
[33] Zhang, F.; Shi, W.; Luo, J.; Pellet, N.; Yi, C.; Li, X.; Zhao, X.; Dennis, T. J. S.; Li, X.; Wang, S.; Xiao, Y.; Zakeeruddin, S. M.; Bi, D.; Grätzel, M. Isomer-Pure Bis-PCBM-Assisted Crystal Engineering of Perovskite Solar Cells Showing Excellent Efficiency and Stability. *Adv. Mater.* **2017**, *29*, 1606806.
[34] Tian, C.; Betancourt-Solis, G.; Nan, Z.; Liu, K.; Lin, K.; Lu, J.; Xie, L.; Echegoyen, L.; Wei, Z. Efficient and stable inverted perovskite solar cells enabled by inhibition of self-aggregation of fullerene electron-transporting compounds. *Sci. Bull.* **2021**, *66*, 339–346.
[35] Liu, J.; Qiu, L.; Portale, G.; Torabi, S.; Stuart, M. C. A.; Qiu, X.; Koopmans, M.; Chiechi, R. C.; Hummelen, J. C.; Anton Koster, L. J. Side-chain effects on N-type organic thermoelectrics: A case study of fullerene derivatives. *Nano Energy* **2018**, *52*, 183–191.
[36] Leung, F. K.-C.; Ishiwari, F.; Kajitani, T.; Shoji, Y.; Hikima, T.; Takata, M.; Saeki, A.; Seki, S.; Yamada, Y. M. A.; Fukushima, T. Supramolecular Scaffold for Tailoring the Two-Dimensional Assembly of Functional Molecular Units into Organic Thin Films. *J. Am. Chem. Soc.* **2016**, *138*, 11727–11733.
[37] Dong, B. X.; Nowak, C.; Onorato, J. W.; Strzalka, J.; Escobedo, F. A.; Luscombe, C. K.; Nealey, P. F.; Patel, S. N. Influence of Side-Chain Chemistry on Structure and Ionic Conduction Characteristics of Polythiophene Derivatives: A Computational and Experimental Study. *Chem. Mater.* **2019**, *31*, 1418–1429.
[38] Reyes-Reyes, M.; Kim, K.; Carroll, D. L. High-efficiency photovoltaic devices based on annealed poly(3-hexylthiophene) and 1-(3-methoxycarbonyl)-propyl-1-phenyl-(6,6)C_{61} blends. *Appl. Phys. Lett.* **2005**, *87*, 083506.
[39] Jia, L.; Chen, M.; Yang, S. Functionalization of fullerene materials toward applications in perovskite solar cells. *Mater. Chem. Front.* **2020**, *4*, 2256–2282.
[40] Meng, B.; Liu, J.; Wang, L. Oligo(ethylene glycol) as side chains of conjugated polymers for optoelectronic applications. *Polym. Chem.* **2020**, *1*, 1261–1270.
[41] Khadka, D. B.; Shirai, Y.; Yanagida, M.; Noda, T.; Miyano, K. Tailoring the Open-Circuit Voltage Deficit of Wide-Band-Gap Perovskite Solar Cells Using Alkyl Chain-Substituted Fullerene Derivatives. *ACS Appl. Mater. Interfaces* **2018**, *10*, 22074–22082.
[42] Meng, B.; Song, H.; Chen, X.; Xie, Z.; Liu, J.; Wang, L. Replacing Alkyl with Oligo(ethylene glycol) as Side Chains of Conjugated Polymers for Close π–π Stacking. *Macromolecules* **2015**, *48*, 4357–4363.
[43] Chen, X.; Zhang, Z.; Ding, Z.; Liu, J.; Wang, L. Diketopyrrolopyrrole-based Conjugated Polymers Bearing Branched Oligo(Ethylene Glycol) Side Chains for Photovoltaic Devices. *Angew. Chem. Int. Ed.* **2016**, *55*, 10376–10380.
[44] Shao, S.; Abdu-Aguye, M.; Qiu, L.; Lai, L.-H.; Liu, J.; Adjokatse, S.; Jahani, F.; Kamminga, M. E.; ten Brink, G. H.; Palstra, T. T. M.; Kooi, B. J.; Hummelen, J. C.; Antonietta Loi, M. Elimination of the light soaking effect and performance enhancement in perovskite solar cells using a fullerene derivative. *Energ. Environ. Sci.* **2016**, *9*, 2444–2452.
[45] Meng, X.; Bai, Y.; Xiao, S.; Zhang, T.; Hu, C.; Yang, Y.; Zheng, X.; Yang, S. Designing New Fullerene Derivatives as Electron Transporting Materials for Efficient Perovskite Solar Cells with Improved Moisture Resistance. *Nano Energy* **2016**, *30*, 341–346.
[46] Bassaiahgari, A.; Panda, S.; Gardas, R. L. Effect of Ethylene, Diethylene, and Triethylene Glycols and Glycerol on the Physicochemical Properties and Phase Behavior of Benzyltrimethyl and Benzyltributylammonium Chloride Based Deep Eutectic Solvents at 283.15–343.15 K. *J. Chem. Eng. Data* **2018**, *63*, 2613–2627.
[47] Xu, G.; Xue, R.; Chen, W.; Zhang, J.; Zhang, M.; Chen, H.; Cui, C.; Li, H.; Li, Y.; Li, Y. New Strategy for Two-Step Sequential Deposition: Incorporation of Hydrophilic Fullerene in Second Precursor for High-Performance p-i-n Planar Perovskite Solar Cells. *Adv. Energ Mater.* **2018**, *8*, 1703054.
[48] Yan, K.; Chen, J.; Ju, H.; Ding, F.; Chen, H.; Li, C.-Z. Achieving high-performance thick-film perovskite solar cells with electron transporting Bingel fullerenes. *J. Mater. Chem. A* **2018**, *6*, 15495–15503.
[49] Xu, G.; Wang, S.; Bi, P.; Chen, H.; Zhang, M.; Xue, R.; Hao, X.; Wang, Z.; Li, Y.; Li, Y. Hydrophilic Fullerene Derivative Doping in Active Layer and Electron Transport Layer for Enhancing Oxygen Stability of Perovskite Solar Cells. *Solar RRL* **2020**, *4*, 1900249.
[50] Collavini, S.; Saliba, M.; Tress, W. R.; Holzhey, P. J.; Völker, S. F.; Domanski, K.; Turren-Cruz, S. H.; Ummadisingu, A.; Zakeeruddin, S. M.; Hagfeldt, A.; Grätzel, M.; Delgado, J. L. Poly(ethylene glycol)–[60]Fullerene-Based Materials for Perovskite Solar Cells with Improved Moisture Resistance and Reduced Hysteresis. *ChemSusChem* **2018**, *11*, 1032–1039.
[51] Tian, C.; Sun, C.; Chen, J.; Song, P.; Hou, E.; Xu, P.; Liang, Y.; Yang, P.; Luo, J.; Xie, L.; Wei, Z. Fullerene Derivative with Flexible Alkyl Chain for Efficient Tin-Based Perovskite Solar Cells. *Nanomaterials* **2022**, *12*, 532.
[52] Wang, X.; Fan, Y.; Wang, L.; Chen, C.; Li, Z.; Liu, R.; Meng, H.; Shao, Z.; Du, X.; Zhang, H.; Cui, G.; Pang, S. Perovskite Solution Aging: What Happened and How to Inhibit? *Chem* **2020**, *6*, 1369–1378.
[53] Valenzano, V.; Cesari, A.; Balzano, F.; Milella, A.; Fracassi, F.; Listorti, A.; Gigli, G.; Rizzo, A.; Uccello-Barretta, G.; Colella, S. Methylammonium-formamidinium reactivity in aged organometal halide perovskite inks. *Cell Rep. Phys. Sci.* **2021**, 100432.
[54] Saliba, M.; Matsui, T.; Domanski, K.; Seo, J.-Y.; Ummadisingu, A.; Zakeeruddin, S. M.; Correa-Baena, J.-P.; Tress, W. R.; Abate, A.; Hagfeldt, A.; Grätzel, M. Incorporation of rubidium cations into perov-

skite solar cells improves photovoltaic performance. *Science* **2016**, *354*, 206–209.
[55] Gao, B.; Meng, J. RbCs(MAFA)PbI_3 perovskite solar cell with 22.81% efficiency using the precise ions cascade regulation. *Appl. Surface Sci.* **2020**, *530*, 147240.
[56] Fernandez-Delgado, O.; Chandrasekhar, P. S.; Cano-Sampaio, N.; Simon, Z. C.; Puente-Santiago, A. R.; Liu, F.; Castro, E.; Echegoyen, L. The role of fullerene derivatives in perovskite solar cells: electron transporting or electron extraction layers? *J. Mater. Chem. C* **2021**, *9*, 10759–10767.
[57] Elnaggar, M.; Elshobaki, M.; Mumyatov, A.; Luchkin, S. Y.; Dremova, N. N.; Stevenson, K. J.; Troshin, P. A. Molecular Engineering of the Fullerene- Based Electron Transport Layer Materials for Improving Ambient Stability of Perovskite Solar Cells. *Solar RRL* **2019**, *3*, 1900223.
[58] Hu, H.; Moghadamzadeh, S.; Azmi, R.; Li, Y.; Kaiser, M.; Fischer, J. C.; Jin, Q.; Maibach, J.; Hossain, I. M.; Paetzold, U. W.; Abdollahi Nejand, B. Sn-Pb Mixed Perovskites with Fullerene-Derivative Interlayers for Efficient Four-Terminal All-Perovskite Tandem Solar Cells. *Adv. Funct. Mater.* **2022**, *32*, 2107650.
[59] Wu, C.; Wang, K.; Yan, Y.; Yang, D.; Jiang, Y.; Chi, B.; Liu, J.; Esker, A. R.; Rowe, J.; Morris, A. J.; Sanghadasa, M.; Priya, S. Fullerene Polymer Complex Inducing Dipole Electric Field for Stable Perovskite Solar Cells. *Adv. Funct. Mater.* **2019**, *29*, 1804419.
[60] Przypis, L.; Ahmad, T.; Misztal, K.; Honisz, D.; Radicchi, E.; Mosconi, E.; Domagala, W.; De Angelis, F.; Wojciechowski, K. Designing New Indene- Fullerene Derivatives as Electron-Transporting Materials for Flexible Perovskite Solar Cells. *J. Phys. Chem. C* **2021**, *125*, 27344–27353.
[61] Wang, S.; Chen, H.; Zhang, J.; Xu, G.; Chen, W.; Xue, R.; Zhang, M.; Li, Y.; Li, Y. Targeted Therapy for Interfacial Engineering Toward Stable and Efficient Perovskite Solar Cells. *Adv. Mater.* **2019**, *31*, 1903691.
[62] Jahani, F.; Torabi, S.; Chiechi, R. C.; Koster, L. J. A.; Hummelen, J. C. Fullerene derivatives with increased dielectric constants. *Chem. Commun.* **2014**, *50*, 10645–10647.
[63] Ghosh, S.; Pal, S. K.; Karki, K. J.; Pullerits, T. Ion Migration Heals Trapping Centers in $CH_3NH_3PbBr_3$ Perovskite. *ACS Energ. Lett.* **2017**, *2*, 2133–2139.
[64] Fu, X.; Jacobs, D. A.; Beck, F. J.; Duong, T.; Shen, H.; Catchpole, K. R.; White, T. P. Photoluminescence study of time- and spatial-dependent light induced trap de-activation in $CH_3NH_3PbI_3$ perovskite films. *Phys. Chem. Chem. Phys.* **2016**, *18*, 22557–22564.
[65] deQuilettes, D. W.; Zhang, W.; Burlakov, V. M.; Graham, D. J.; Leijtens, T.; Osherov, A.; Bulović, V.; Snaith, H. J.; Ginger, D. S.; Stranks, S. D. Photo-induced halide redistribution in organic–inorganic perovskite films. *Nat. Commun.* **2016**, *7*, 11683.
[66] Tian, Y.; Peter, M.; Unger, E.; Abdellah, M.; Zheng, K.; Pullerits, T.; Yartsev, A.; Sundström, V.; Scheblykin, I. G. Mechanistic insights into perovskite photoluminescence enhancement: light curing with oxygen can boost yield thousandfold. *Phys. Chem. Chem. Phys.* **2015**, *17*, 24978–24987.
[67] Wong, K. K.; Fakharuddin, A.; Ehrenreich, P.; Deckert, T.; Abdi-Jalebi, M.; Friend, R. H.; Schmidt-Mende, L. Interface-Dependent Radiative and Nonradiative Recombination in Perovskite Solar Cells. *J. Phys. Chem. C* **2018**, *122*, 10691–10698.

Manuscript received: August 20, 2022
Manuscript revised: October 11, 2022
Manuscript accepted: October 24, 2022
Accepted manuscript online: October 28, 2022
Version of record online: January 3, 2023

The Authors

Left to Right:
Top panel: Tobias Seewald, Emilia R. Schütz, Lukas Schmidt-Mende, Azhar Fakharuddin, Georgios C. Vougioukalakis, Leandros P. Zorba, Polychronis Tsipas, Anastasia Soultati, Maria Vasilopoulou,
Bottom panel: Konstantina-Kalliopi Armadorou, Marinos Tountas, Nikolaos Tzoganakis, Stylianos Panagiotakis, Emmanuel Kymakis, Abd Rashid bin Mohd Yusoff, Konstantinos Aidinis, Mohammad Khaja Nazeeruddin

